



Molecular dynamics simulation of crack growth in nanocrystalline nickel considering the effect of accumulated plastic deformation

Yifan Yu^{a,*}, Yipeng Rao^b

^a School of Aerospace Engineering, Tsinghua University, Beijing 100084, China

^b Institute for Computing and Digital Economy, Peking University, Changsha 410205, China



ARTICLE INFO

Keywords:

Molecular dynamics
Crack propagation
Micro-nanoscale
Atomic stress
Plastic strain
Strain concentration factor

ABSTRACT

Molecular dynamics simulations are conducted to investigate atomic stress and plastic strain distribution in pre-cracked crystalline nickel, along with microstructure evolution. The plastic strain calculation method is improved by refining neighboring atom selection. A new parameter for measuring plastic strain concentration allows for comparison across different crystallographic directions. The effects of temperature, strain rate, crystallographic direction, loading mode, grain boundary and grain size are evaluated. At elevated temperature, crack tip blunting becomes obvious, and crack propagation decelerates. The crack propagates through void nucleation, growth, and eventual linkage with the original crack. Higher temperature increases the plasticity limit of void nucleation. Strain rates show a positive correlation with plasticity limit but a negative correlation with crack growth rate and final length. Crystallographic direction influences crack propagation, with crystal $\langle 100 \rangle$ exhibiting significant crack propagation, while $\langle 110 \rangle$ and $\langle 111 \rangle$ demonstrating marked resistances to crack propagation. Crystal $\langle 100 \rangle$ has the highest plastic deformation concentration near the crack tip. Loading mode affects plastic deformation accumulation. In-plane shear results in less plastic deformation and less obvious crack propagation. In bi-crystals, the relative rotation angle between grains significantly influences crack propagation. X-rotation of the right grain most significantly impedes crack propagation, while y- and z-rotation tend to cause the crack to cross the grain boundary. In polycrystals, plastic deformation accumulation at grain boundaries is significant, with the crack tending to propagate along grain boundaries. Plastic strain and concentration parameter peaks are lower in grain boundaries than in single crystals, indicating weaker stability. The results demonstrate that the failure process of crystalline nickel is intricately linked to the stress and plastic strain distribution around the crack tip. The plastic strain and concentration parameter are more accurate predictors of crack propagation than atomic stress.

1. Introduction

The fracture phenomenon at the macroscale is a multi-scale process, initiated at the microscale by atomic bond disruption and crack propagation under external loads. The external loads generate stress fields that drive the bond breaking, influenced by factors such as crystallographic direction, temperature, loading rate and internal conditions (e.g., voids, dislocations and grain boundaries). Understanding these mechanisms is crucial for designing and manipulating material microstructures to optimize properties.

Molecular dynamics (MD) simulations provide a powerful approach for exploring fracture behaviors at the atomic level, offering insights into the mechanical properties and microstructure evolution of

materials. Over recent years, numerous studies have utilized MD to investigate crack propagation, highlighting the significant role of atomic stress in micro-nanoscale fractures. For instance, Nishimura and Miyazaki [1] analyzed the atomic arrangement and stress distribution at the crack tip in alpha-iron (α -Fe), finding that the fatigue crack propagation occurs through the coalescence of the crack and voids. Buehler et al. [2] investigated the stress and strain fields near the crack tip, and compared the results with the asymptotic continuum mechanics predictions, confirming the applicability of continuum mechanics to nanoscale dynamic problems. Matsumoto et al. [3] presented MD simulations of crack propagation in an amorphous metal, examining internal structural changes around the crack tip and their impact on crack growth behaviors and deformation states. Karimi et al. [4] explored crack propagation

* Corresponding author.

E-mail address: yuyifan@lsecc.ac.cn (Y. Yu).

under mode I loading in a nickel (Ni) single crystal with and without defects, noting that the critical strain required for crack propagation depends on the defect configuration. Guo and Zhao [5] observed twinning, recrystallization, and grain nucleation around the crack tip in body-centered cubic iron (BCC Fe) at low temperatures, while Guo et al. [6,7] further examined the mechanisms of martensitic phase transformation and recrystallization in BCC Fe, finding significant effects of local stress and crystallographic direction on these processes. Xu and Deng [8] focused on nanoscale crack growth within an aluminum (Al) single crystal, particularly on the stress evolution surrounding the crack tip, where they observed a significant concentration of atomic stress just before void nucleation. Krull and Yuan [9] studied the cohesive traction-separation law using constrained three-dimensional atomistic simulations, revealing a pattern of void nucleation, growth, and coalescence similar to ductile fracture at the mesoscale. Wu and Yao [10] analyzed the microstructure evolution and stress distribution characteristics of pre-cracked single-crystal Ni at different temperatures, demonstrating that the crack growth process and stress distribution vary with ambient temperature and the surrounding microstructures. Zhang [11] developed a mechanistic model of deformation in a crystalline material with a crack, showing good quantitative alignment of material softening and hardening behaviors with MD simulation results. Ma et al. [12] investigated the effect of crystallographic orientation on fatigue crack propagation, discovering variations in crack growth rate and slip direction based on orientation, and noted that different grain boundaries exhibit varied resistance to crack propagation. Sung and Chen [13] employed MD simulations to explore the crack growth process in pre-cracked Ni subjected to the mode I loading, finding that critical stress significantly depends on crystallographic orientation. Qiu et al. [14] studied the mechanical properties and crack propagation behavior of polycrystalline copper (Cu), focusing on the effects of temperature, grain size, and crack length. Ji et al. [15] evaluated the interaction between cracks and the crack propagation in crystalline aluminum (Al), assessing the influence of the crack size and spacing on material fracture properties. Liu et al. [16] investigated phase transformations in high-entropy alloys under various stress states, linking these transformations to crack propagation dynamics.

Plastic deformation is a critical aspect of material science and engineering, significantly influencing the mechanical properties of materials such as strength, ductility, and toughness. Excessive local plastic deformation can destabilize the lattice structure, forming a fracture process zone characterized by nonlinear and dissipative mechanisms [17,18]. This zone profoundly affects crack-related phenomena including initiation, growth, propagation, branching, interaction, coalescence, and merging [19]. Despite its undeniable importance, research on the impact of accumulated plastic strain on crack propagation based on MD simulations remains insufficient. Previous studies on plastic deformation have primarily focused on qualitative analyses, tracking microstructural evolution rather than quantitatively assessing the distribution and progression of plastic deformation alongside crack propagation. Furthermore, most MD studies on crack propagation emphasize atomic stress distribution, yet stress peaks occur not only at void nucleation sites but also near other defects like twin boundaries and dislocations [20–23]. This complexity makes understanding crack propagation and material fracture properties through changes in the stress field challenging. To address these limitations, we have developed an algorithm for calculating plastic deformation at the atomic scale [24], which we now apply to analyze the impact of plastic deformation on crack propagation more quantitatively. This algorithm aims to enhance our understanding of micro-nanoscale fracture mechanisms, emphasizing that a sole focus on stress is insufficient and the role of plastic deformation must be considered.

In this paper, we enhance existing methods for calculating atomic strain and introduce a new algorithm for calculating plastic deformation. Additionally, we propose a parametric approach to quantify the concentration of plastic strain. We then conduct MD simulations to

explore the crack growth process in pre-cracked nickel (Ni) plates under various conditions, including temperatures, loading rates, and crystallographic directions, as well as in bi-crystalline and polycrystalline environments. This study aims to thoroughly examine the mechanisms of crack growth and failure in face-centered cubic (FCC) crystals by analyzing defect structures, plastic strain, and stress fields around the crack tip.

The remainder of this paper is structured as follows: Section 2 details the models and calculation methods for MD simulations of crack propagation. Section 3 presents results and discussions of crack propagation under various conditions, including temperatures (subsection 3.1), loading rates (subsection 3.2), crystallographic directions (subsection 3.3), loading modes (subsection 3.4), bi-crystals (subsection 3.5), and polycrystals (subsection 3.6). Section 4 concludes the paper with a summary of findings.

2. Model and methodology

2.1. Atomistic models and simulation process

Fig. 1 shows the detailed geometry of the models. The pre-crack is positioned on the left side, with model dimensions: $-50a \leq x \leq 50a$, $-50a \leq y \leq 50a$, $-5a \leq z \leq 5a$. The initial crack has a length of $10a$ and a width of $2a$, where a (3.52 \AA) represents the Ni lattice constant. The top and bottom layers have a width of $2a$, and the left and right layers are wide. The models undergo loading in both mode I and II. In mode I, external forces are applied vertically (y -direction) on top and bottom layers, marked by blue arrows. In mode II, forces are applied horizontally (x -direction) on upper left and lower left layers, marked by red arrows. The quasi-static loading method is adopted. After each incrementally loading, the entire system is subsequently relaxed at the desired external temperature using NVT ensemble (temperature T , volume V , number of the atoms N). Periodic boundary conditions are implemented in the z -direction, with non-periodic boundary conditions in the x - and y -directions. The left and right boundaries are constrained in the x -direction to minimize boundary effects.

Three type models of pre-cracked nickel (Ni) are constructed for molecular simulations of crack propagation, as shown in **Fig. 1**. Type I models include the single crystal Ni models A, B and C, with different crystal orientations. The model A is orientated [100], [010] and [001], along the x , y - and z -axes, respectively; The model B is orientated [001], [110] and $[\bar{1}10]$; The model C is orientated $[1\bar{1}\bar{2}]$, $[111]$ and $[1\bar{1}\bar{0}]$. These models investigate the influence of temperature (0 K, 30 K, 300 K),

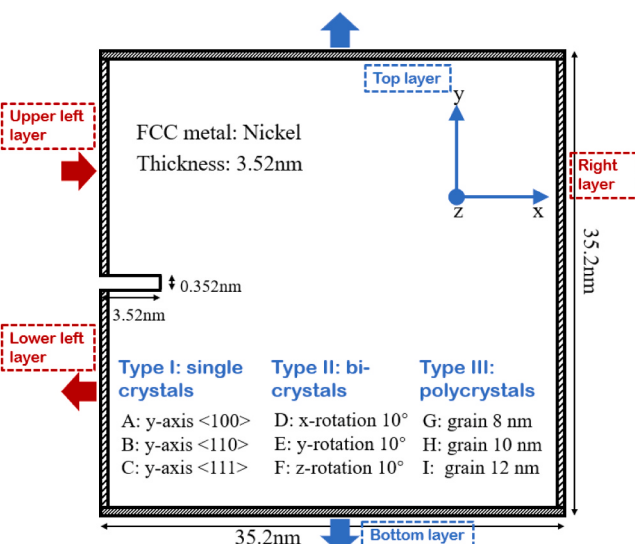


Fig. 1. Geometry of the simulated system of a single crystal with an edge crack.

strain rate (2.0×10^8 – 2.0×10^9), crystallographic direction of loading ($\langle 010 \rangle$, $\langle 110 \rangle$, $\langle 111 \rangle$) and loading mode (tension and shear) on crack growth and structural failure of single-crystal Ni. Type II models include the bi-crystal models D, E and F. These models have two grains with distinct orientations, forming the grain boundaries in the middle. In model D, the right grain is rotated 10° around the x-axis relative to the left grain. In model E, it is rotated 10° around the y-axis, and in model F, it is 10° around the z-axis. These models are used to assess the impact of grain boundaries on crack propagation. Type III models consist of the polycrystalline models F, G and H, with grain sizes of 8, 10 and 12 nm. These models are generated using the Voronoi Tessellation algorithm, with each Voronoi cell's crystal orientation randomly determined. Type III models explore the effects of grain size on structural behavior.

The MD simulations are performed by the open-source software the large-scale atomic/molecular massively parallel simulator (LAMMPS) [21]. The atomic interactions in Ni are described by an accurate embedded atom method (EAM) potential developed by [20]. The open visualization tool (OVITO) [25] is used to visualize the simulation results.

2.2. Stress calculation

The virial stress tensor of atom i in its occupied volume is calculated by

$$\boldsymbol{\sigma}_i = -\frac{1}{V_i} m_i \mathbf{v}_i \otimes \mathbf{v}_i - \frac{1}{2V_i} \sum_{j=1}^{n_i} \mathbf{r}_{ji} \otimes \mathbf{f}_{ji}, \quad (1)$$

where m_i is the mass of atom i , \mathbf{v}_i is the velocity, V_i is the atom-occupied volume [26], \mathbf{f}_{ji} is the interaction force exerted by atom j on i , \mathbf{r}_{ji} is the relative position from atom j to i , n_i is the number of neighbors of atom i within the cut-off distance of the EAM potential, Ni has a cut-off distance of 4.80 Å [10].

The average atomic stress tensor of atom i within the potential cut-off distance is given by

$$\bar{\boldsymbol{\sigma}}_i = \frac{1}{n_i + 1} \left(\sum_{j=1}^{n_i} \boldsymbol{\sigma}_j + \boldsymbol{\sigma}_i \right), \quad (2)$$

where $\boldsymbol{\sigma}_i$ is the atomic stress of center i , and $\boldsymbol{\sigma}_j$ is the atomic stress of neighbors. In fracture mechanics, stress triaxiality is an essential dimensionless parameter for analyzing material failure. However, Krull and Yuan [9] emphasized that at the microscale, damage in crystals with cracks predominantly stems from normal stress. Their findings suggested that void nucleation and crack growth are driven by concentrations of atomic tensile stress and hydrostatic stress, and the effects of these two stresses are positively correlated. Simultaneously, numerical experiments from [9] demonstrated that the peaks and valleys of tensile stress are more distinctly evident in stress contour plots. Moreover, tensile stress is widely employed to investigate the crack growth behavior [10,20–23,27]. Therefore, this paper primarily focuses on the y-direction stress σ_{yy} and strain E_{yy} .

2.3. Atomic strain calculation

Calculation of atomic strain requires two atomic configurations, reference \mathcal{B}_0 , and current \mathcal{B}_1 . A local deformation gradient \mathbf{F}_i that best maps is calculated

$$\{\mathbf{R}_{ij}\} \rightarrow \{\mathbf{r}_{ij}\}, \forall j \in D_i^0 \cap D_i^1, \quad (3)$$

where D_i^0 and D_i^1 are the neighbors of atom i in \mathcal{B}_0 and \mathcal{B}_1 respectively, \mathbf{R}_{ij} and \mathbf{r}_{ij} are the relative atomic positions in \mathcal{B}_0 and \mathcal{B}_1 , and atom j is one of the neighbors.

Our method deviates from the standard atomic strain approach,

which typically select the an atom's neighbors based on the reference configuration [28,29]. This traditional method is not effective for large deformations and fractures, as reference neighbors may become distant from the central atom post-deformation, diminishing their interactions. Therefore, our improved method selects neighbors for the central atom in both the reference and current configurations, ensuring that the calculation of central-atom strain accurately reflects the actual proximity between atoms.

The local deformation gradient \mathbf{F}_i is determined by minimizing

$$\sum_{j \in D_i^0 \cap D_i^1} |\mathbf{F}_i \mathbf{R}_{ij} - \mathbf{r}_{ij}|^2 \rightarrow \mathbf{F}_i = \left(\sum_{j \in D_i^0 \cap D_i^1} \mathbf{r}_{ij} \mathbf{R}_{ij}^T \right) \left(\sum_{j \in D_i^0 \cap D_i^1} \mathbf{R}_{ij} \mathbf{R}_{ij}^T \right)^{-1}. \quad (4)$$

The local Green-Lagrangian strain \mathbf{E}_i is computed

$$\mathbf{E}_i = \frac{1}{2} (\mathbf{F}_i^T \mathbf{F}_i - \mathbf{I}). \quad (5)$$

The average atomic strain tensor of atom i within the cut-off distance of EAM potential is given by

$$\bar{\mathbf{E}}_i = \frac{1}{n_i + 1} \left(\sum_{j=1}^{n_i} \mathbf{E}_j + \mathbf{E}_i \right), \quad (6)$$

where n_i is the number of current neighbors of atom i .

2.4. Plastic deformation

The plastic deformation is calculated by the method proposed in [24]. Fig. 2 shows the elastic-plastic decomposition of a deformation gradient between the reference configuration \mathcal{B}_0 and the current configuration \mathcal{B}_1 . \mathcal{L}_1 represents the unloaded configuration of \mathcal{B}_1 . The deformation gradient of $\mathcal{B}_0 \rightarrow \mathcal{L}_1$ is the plastic component of the total deformation gradient of $\mathcal{B}_0 \rightarrow \mathcal{B}_1$. Once the intermediated configuration \mathcal{L}_1 is obtained, the plastic strain can be calculated by the atomic strain calculation method mentioned in the previous subsection.

The unloaded configuration \mathcal{L}_1 is obtained by the constrained minimization [24]

$$\begin{aligned} \text{Min}_{\mathbf{u}_1, \mathbf{u}_2, \dots, \mathbf{u}_n} U(\mathbf{r}_1 + \mathbf{u}_1, \mathbf{r}_2 + \mathbf{u}_2, \dots, \mathbf{r}_n + \mathbf{u}_n), \\ \text{Subject to } \mathbf{u}_{p_k} = \mathbf{M}_k(\mathbf{r}_{p_k} - \mathbf{r}_{T_k}) + \mathbf{u}_{T_k} - \mathbf{r}_{p_k} + \mathbf{r}_{T_k}, \\ P_k \in \omega_k, T_k \in \omega_k, 1 \leq k \leq m, \end{aligned} \quad (7)$$

where \mathbf{r}_i is an atom position, \mathbf{u}_i is the atom translation vector, n is the atom number, m is the dislocation number, k is a dislocation, ω_k is an atom group around dislocation k , which is applied to the rigid body constraint, T_k is the reference point of ω_k , generally the centroid, P_k is any point in ω_k , \mathbf{M}_k is the rotation transformation matrix of ω_k .

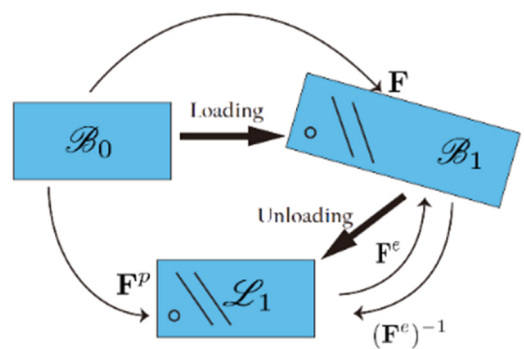


Fig. 2. The elastic–plastic decomposition of a deformation gradient, black lines and circles represent defects.

2.5. Local strain concentration factor

The range of plastic strain values differs across structural models, influenced by factors such as crystal orientations and grain sizes. The plastic strain value alone is insufficient to accurately predict crack propagation behavior across different models. It is also crucial to consider the local concentration of plastic strain to quantitatively assess the likelihood of void nucleation near the crack tip.

According to the definition of stress concentration factor, the local strain concentration factor is defined

$$\kappa_i = \left| \frac{E_i}{\bar{E}_i} \right|, \quad (8)$$

where κ_i represents the strain concentration around atom i , E_i represents the strain at atom i , \bar{E}_i this represents the corresponding average strain. Here, we are concerned with the y-direction normal strain. This factor provides a parametric tool to study the void nucleation in different models at a unified level.

3. Results and discussions

3.1. Temperature effect on crack growth process

We examined the temperature effect on model A at three different temperatures: 10^{-2} (approximately 0), 30 and 300 K. for model A. The strain load was applied in the y-direction, at a rate of $2.0 \times 10^8 \text{ s}^{-1}$. Fig. 3 shows the crack propagation in model A at 0 K, where (a)(b)

shows the average y-direction tensile stress and von Mises stress at 300 ps. The inset represents the CNA results, where green represent FCC and white represent other structures. At low temperatures, dislocations hardly glided and new dislocations were rarely generated, resulting in minimal plastic deformation. With increasing load, the crack propagated rapidly, predominantly forming nearly flat atomic surfaces, and exhibited brittle behavior. After propagating a significant distance (300 ps), no new microstructures emerged at or around the crack tip. Throughout the propagation, the y-direction tensile stress concentrated at the tip, whereas the von Mises stress concentrated along the sides of the path, indicating its unsuitability for studying crack propagation behavior, as noted in [9]. Fig. 3(c) and (d) compare different strain calculation methods; (d) uses the standard method, which only involves neighboring atoms in the reference configuration and incorrectly yields the highest strain values at the crack sides. In contrast, our modified method in (c), also considers neighboring atoms in the current configuration, obtaining a more reasonable result: the maximum strain at the crack tip.

At different temperatures, the evolution of the atomic configuration during stretching changed notably. With the temperature rising, thermal effects enhanced atomic mobility, facilitating dislocation nucleation and glide. Fig. 4 shows the crack propagation of model A at 30 K. Fig. 4(a) shows the CNA result at the blunting (184 ps), where green, blue, red and white represent FCC, BCC, HCP and other structures respectively. The initial microstructures near the crack tip were altered due to dislocation nucleation and emission. Fig. 4(d)(g) show the atomic stress and plastic strain distribution at blunting (184 ps), with the maximum

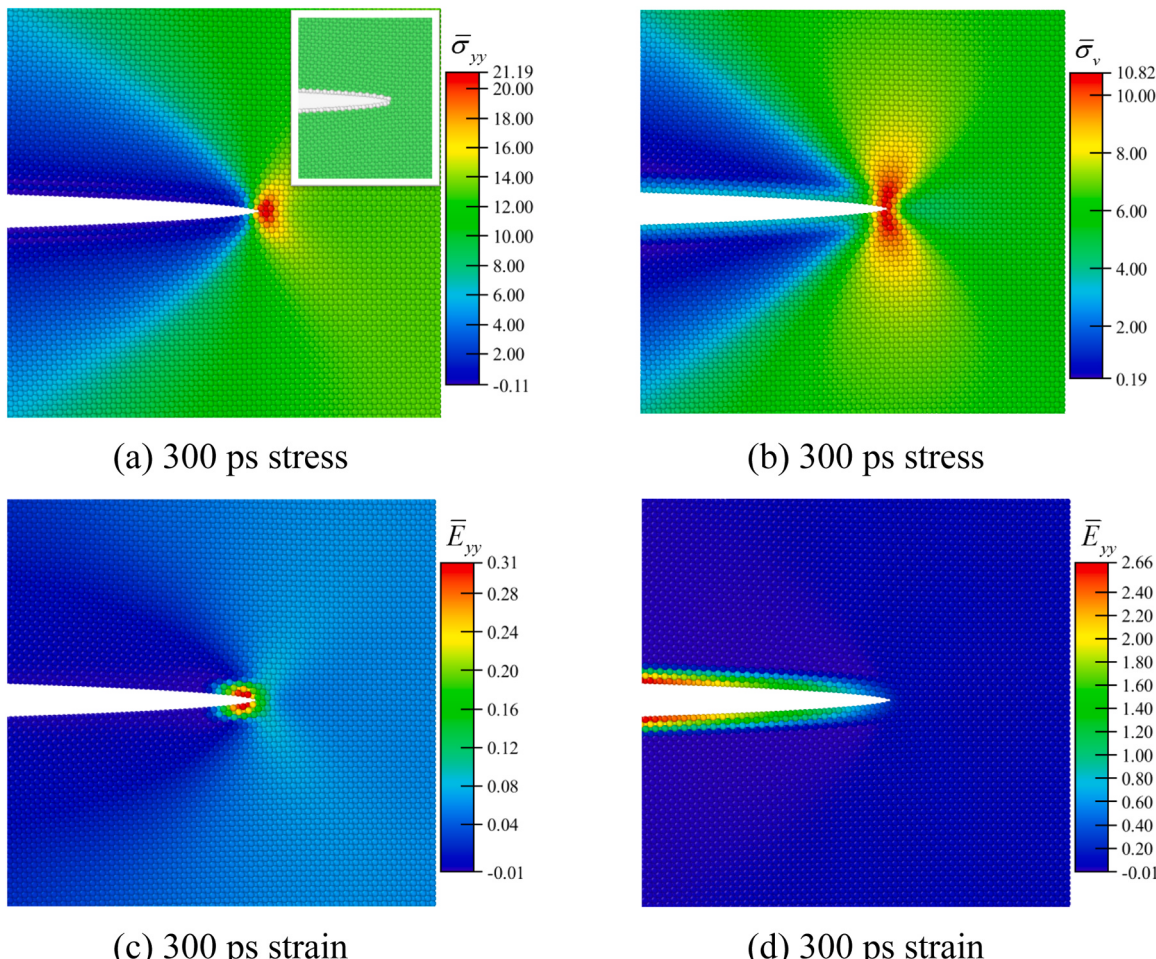


Fig. 3. At 0 K, the crack growth results. (a) Y-direction tensile stress at 300 ps, with a inset displaying the CNA result, (b) the von Mises stress at 300 ps, (c) y-direction strain calculated by our method at 300 ps, (d) y-direction strain calculated by the standard method at 300 ps.

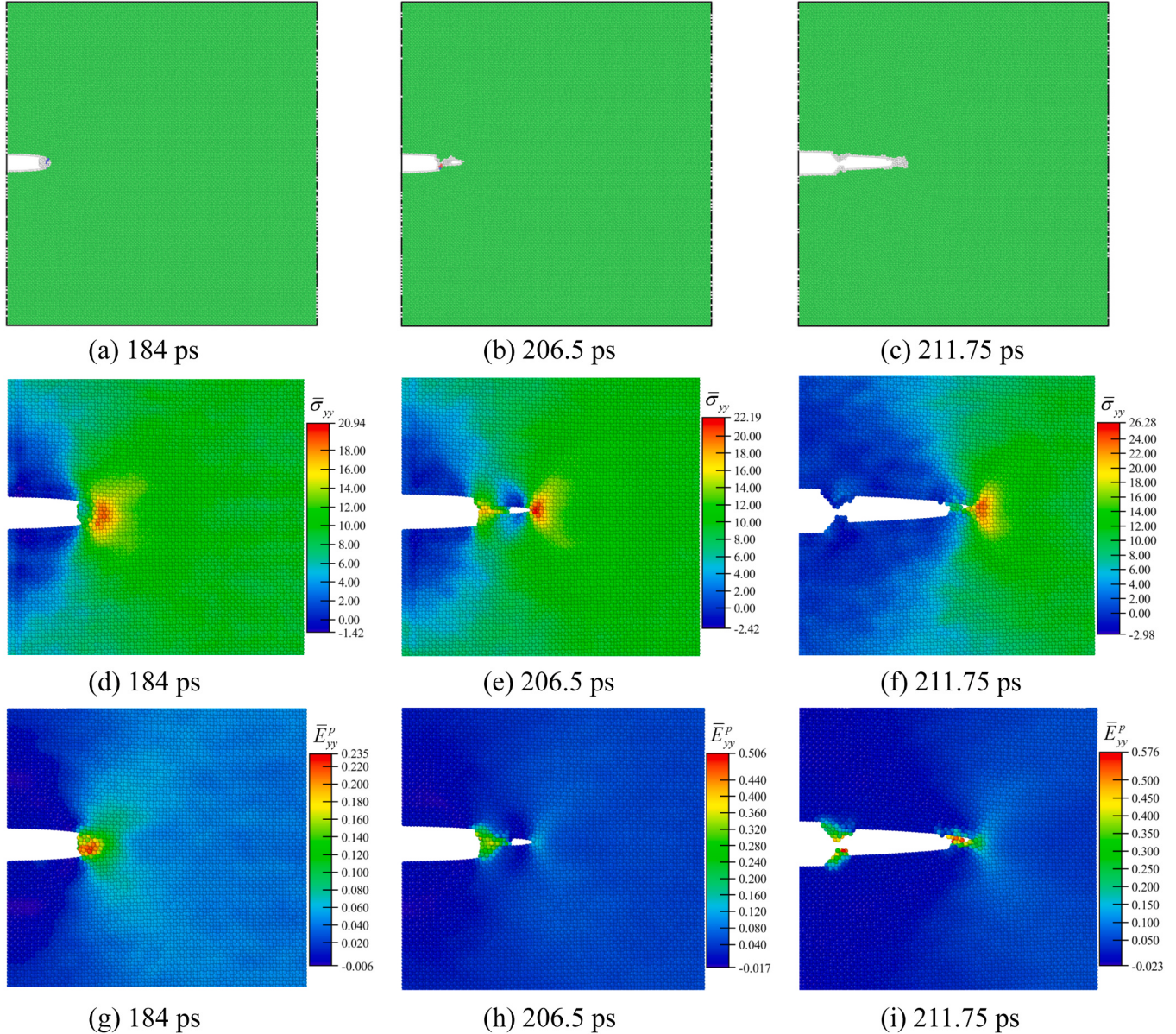


Fig. 4. At 30 K, the crack growth results. (a) CNA at 184 ps, (b) CNA at 206.5 ps, (c) CNA at 211.75 ps, (d) stress at 184 ps, (e) stress at 206.5 ps, (f) stress at 211.75 ps, (g) plastic strain at 184 ps, (h) plastic strain at 206.5 ps, (i) plastic strain at 211.75 ps.

stress and plastic strain recorded at 20.94 GPa and 0.235. As the load intensified, dislocations emitted continuously from the crack tip, yet their mobility was constrained, leading to plastic strain accumulation around the tip. Once the local plastic strain reached the limit, the microstructures began to fracture. Fig. 4(b)(e)(h) capture the first void formation at 206.5 ps, with a maximum stress of 22.19 GPa and plastic strain of 0.506. The maximum stress was basically the same as that at the bunting (184 ps), but the maximum plastic strain was larger. This indicated that the stress concentration at the tip was alleviated through ongoing dislocation emission and the microstructures near the crack tip at 184 ps retained a capacity for plastic deformation. As loading continued, the first void grew and connected to the crack, subsequently leading to the formation of a new void. At 30 K, the crack propagated by void growth, coalescence and connection with the original crack repeatedly, indicative of ductile fracture behavior. Fig. 4(c)(f)(i) shows a new void at 211.75 ps, where the part of $-12.4 \text{ \AA} < z < 0 \text{ \AA}$ is hidden for display clarity. The maximum stress was 26.28 GPa and plastic strain was 0.576, comparable to the initial void generation. Defect structures around the tip contributed to higher stress levels at 30 K compared to

0 K, accompanied by significant plastic deformation. Stress and plastic strain values during void generation—approximately 22 GPa and 0.5, respectively—represent limit values during crack propagation. Continued loading (around 240 ps) increased dislocation mobility, leading to the formation of slip bands along {111} planes, which impeded further crack growth.

Fig. 5 shows the crack growth process of model A at 300 K. Fig. 5(a) shows the plastic blunting around the crack tip at 210 ps, colored by CNA method. Fig. 5(b) shows the first void generation at 280 ps, where the $z > 8 \text{ \AA}$ hidden for clarity. Fig. 5(c) shows another new void generation at 284 ps. At 300 K, crack propagation slowed significantly compared to 0 K and 30 K, indicating enhanced ductility in model A. Notably, slip bands along {111} emerged near the crack tip during these void development, delaying further crack propagation. To investigate the microscopic aspects of ductility, the atomic stress and plastic strain distributions around the crack tip were calculated. Fig. 5(d)(e)(f) show the stress fields at the stages of blunting, first void generation and new void generation, respectively. The stress concentrated ahead of the tip and peaked at approximately 22 GPa, slightly lower than at 30 K owing

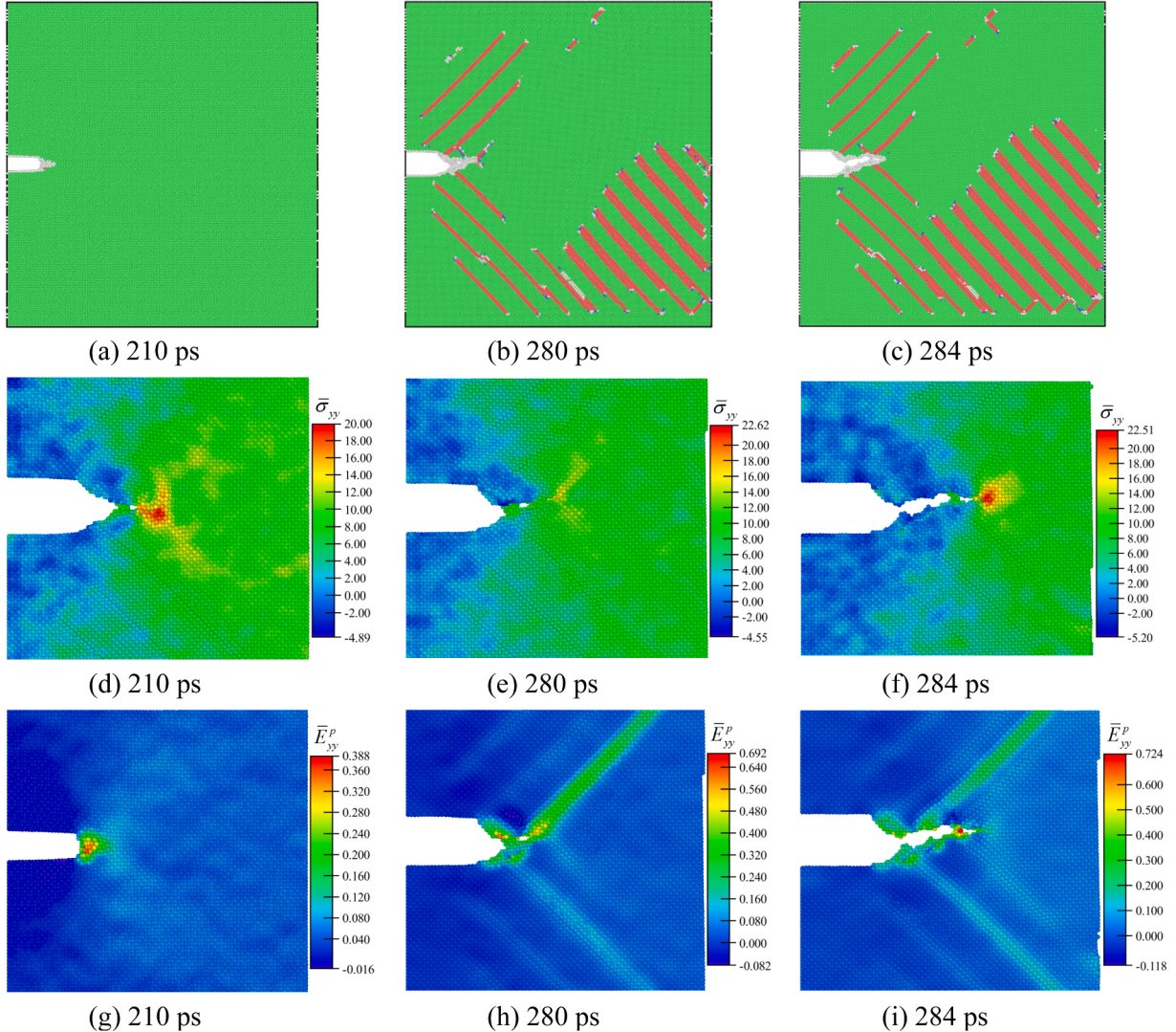


Fig. 5. At 300 K, the crack growth results. (a) CNA at 210 ps, (b) CNA at 280 ps, (c) CNA at 284 ps; (d) stress at 210 ps, (e) stress at 280 ps, (f) stress at 284 ps; (g) plastic strain at 210 ps, (h) plastic strain at 280 ps, (i) plastic strain at 284 ps.

to temperature influence. Fig. 5(g)(h)(i) show the plastic strain fields at these stages. During blunting, the maximum plastic strain was 0.388, and increased to 0.692 and 0.724 at the first and subsequent void generations. At 300 K, the plasticity limit for void generation rose to about 0.700, surpassing that at 30 K. This demonstrated an improvement in the specimen's ductility as the temperature increased, although the stress limit decreased slightly. The results also indicated that void nucleation requires the simultaneous attainment of stress and accumulated plastic deformation at their respective limits.

3.2. Strain rate on crack growth process

To assess the impact of strain rate on the crack growth process, a range of strain rates (2.0×10^8 , 4.0×10^8 , 6.0×10^8 and $2.0 \times 10^9 \text{ s}^{-1}$) were employed in MD simulations for model A at 300 K. For strain rate $2 \times 10^8 \text{ s}^{-1}$, Fig. 5(b) above shows CNA result at the first void generation (280 ps) in model A, where green, blue, red and white represent FCC, BCC, HCP and other structures respectively. Fig. 5(e)(h) show the corresponding stress and plastic strain fields, with maximum values of 22.62 GPa for stress and 0.692 for plastic strain.

Fig. 6 shows the MD simulation results for other strain rates at the first void generation. Fig. 6(a) shows the CNA result for a strain rate of $4 \times 10^8 \text{ s}^{-1}$ at 157 ps, where the parts of $z > 13 \text{ \AA}$ and $z < 10 \text{ \AA}$ are

hidden for clarity. Fig. 6(b) shows the CNA for $8 \times 10^8 \text{ s}^{-1}$ at 71 ps, where $z > 6 \text{ \AA}$ is hidden. Fig. 6(c) shows the CNA for $2 \times 10^9 \text{ s}^{-1}$ at 32 ps, where $z < 9.2 \text{ \AA}$ hidden. As the strain rate increased, the deformation mechanism shifted from dislocation gliding and twinning to predominantly amorphous structure generation, with a marked decrease in the number of slip planes and more localized plastic deformation. Fig. 6(d)(g) show the stress and plastic strain under strain rate $4 \times 10^8 \text{ s}^{-1}$, with maximum values of 20 GPa and 0.799, respectively. Fig. 6(e)(h) show results under strain rate $8 \times 10^8 \text{ s}^{-1}$, with maximum stress and plastic strain of 22.73 GPa and 0.901. Fig. 6(f)(i) show the result under strain rate $2 \times 10^9 \text{ s}^{-1}$, with maximum stress at 19.89 GPa and plastic strain at 1.056. Stress and plastic strain distribution presented a strong correlation with strain rates. Red circles in the Fig. 6(d)–(g) indicate regions of extreme stress and plastic strain, revealing multiple stress peaks, some distant from the crack tip, while plastic strain peak only in one region and close to the crack tip. This pattern suggested that tracking stress peaks alone does not suffice to predict crack propagation behavior accurately. With increasing strain rates, accumulated plastic strain rose during void nucleation, but local stress generally decreased due to the formation of amorphous structures, which reduce material strength and lead to strain softening. The results indicated that for all strain rates, crack initiation conditions still involve surpassing a critical threshold of plastic deformation around the crack tip, coupled

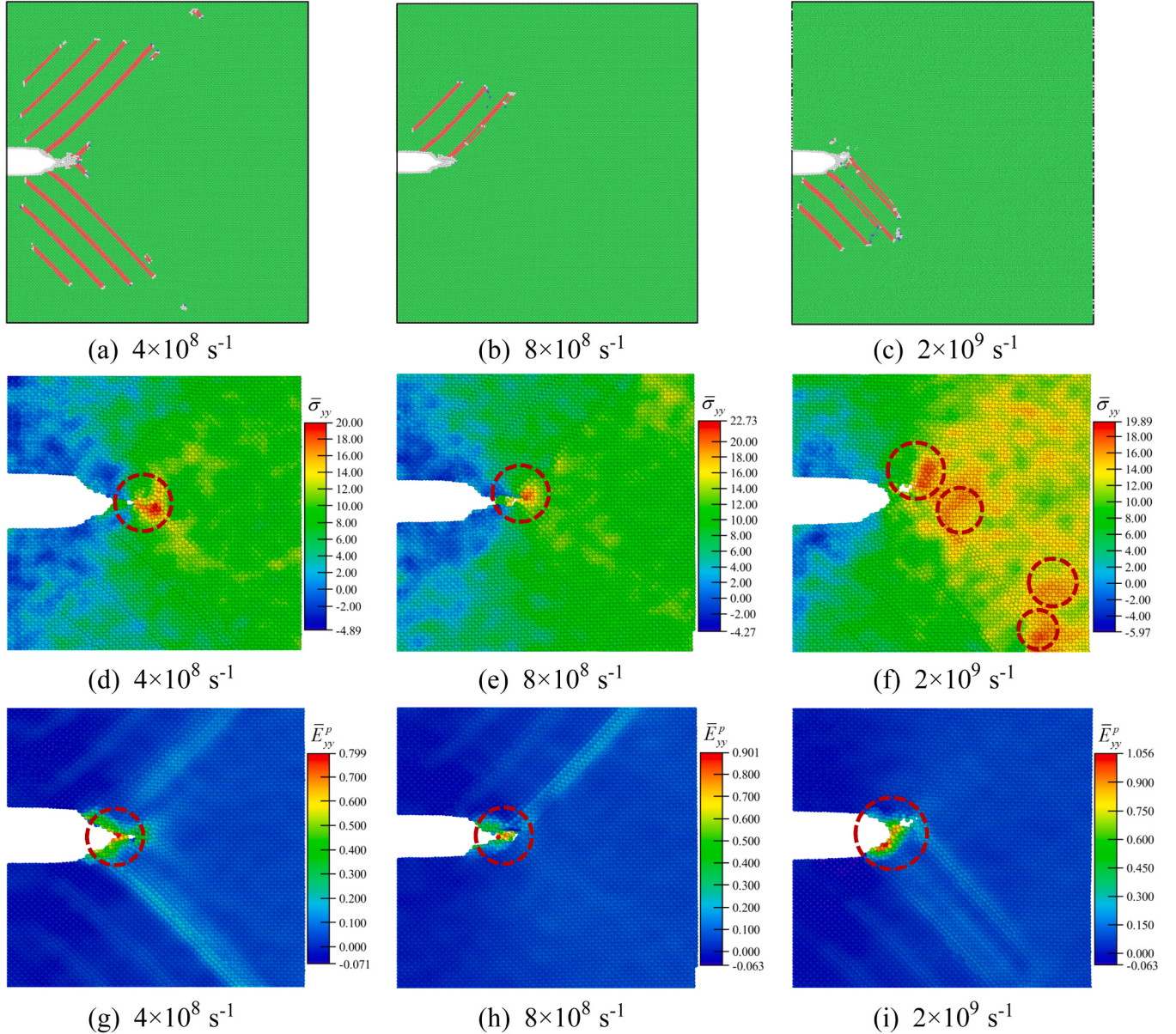


Fig. 6. The crack propagation under different strain rates. (a) CNA under $4 \times 10^8 \text{ s}^{-1}$, (b) CNA under $8 \times 10^8 \text{ s}^{-1}$, (c) CNA under $2 \times 10^9 \text{ s}^{-1}$; (d) stress under $4 \times 10^8 \text{ s}^{-1}$, (e) stress under $8 \times 10^8 \text{ s}^{-1}$, (f) stress under $2 \times 10^9 \text{ s}^{-1}$; (g) plastic strain under $4 \times 10^8 \text{ s}^{-1}$, (h) plastic strain under $8 \times 10^8 \text{ s}^{-1}$, (i) plastic strain under $2 \times 10^9 \text{ s}^{-1}$.

with significant stress concentration on the inner side of the tip.

3.3. Crystallographic direction effect on crack growth process

To investigate the crystalline orientation effect on crack propagation, we performed MD simulations for three different crystallographic direction models A, B and C, y -direction oriented along $\langle 100 \rangle$, $\langle 110 \rangle$ and $\langle 111 \rangle$, respectively. We employed the mode I loading condition with a strain rate of $2 \times 10^8 \text{ s}^{-1}$ at an ambient temperature of 300 K. Fig. 5 above already shows the MD simulation results of model A, (a)(b)(c) show the CNA results of the crack growth process, and (d)–(i) show the corresponding stress and plastic strain distributions. These results demonstrated continuous generation of both perfect and partial dislocations at the crack tip, significant blunting the tip, and some dislocations glided along the closely packed plane $\{111\}$ to the boundaries. Other dislocations entangled ahead of the crack tip, accumulating plastic deformation until the plasticity limit was reached, leading to

evident crack propagation. As the crack propagated, more slip bands were formed and decelerated the crack growth rate.

Fig. 7 shows the MD simulation results of model B and C. Fig. 7(a)(b) show the CNA result of model B at 300 ps, where green, blue, red and white represent FCC, BCC, HCP and other structures respectively. Partial dislocations nucleated at the crack tip crossed the configuration along slip planes $(11\bar{1})$ and $(\bar{1}\bar{1}1)$ with Burgers vectors of $1/6[121]$ and $1/6[\bar{1}21]$. Although no significant slip bands were formed, the presence of stacking faults, twinning structures, and Lomer-Cottrell locks was noted. In model B, substantial crack propagation was absent; with further loading, the crack widened but length remained mostly unchanged, and almost no voids were formed.

Fig. 8 shows the stress, plastic strain and plastic strain concentration factor of model B. Fig. 8(a) reveals that unlike model A, where stress concentration occurred ahead of the crack tip, model B exhibited stress concentration directly at the tip. Moreover, there is no clear correlation between stress distribution and defect distribution, suggesting that using

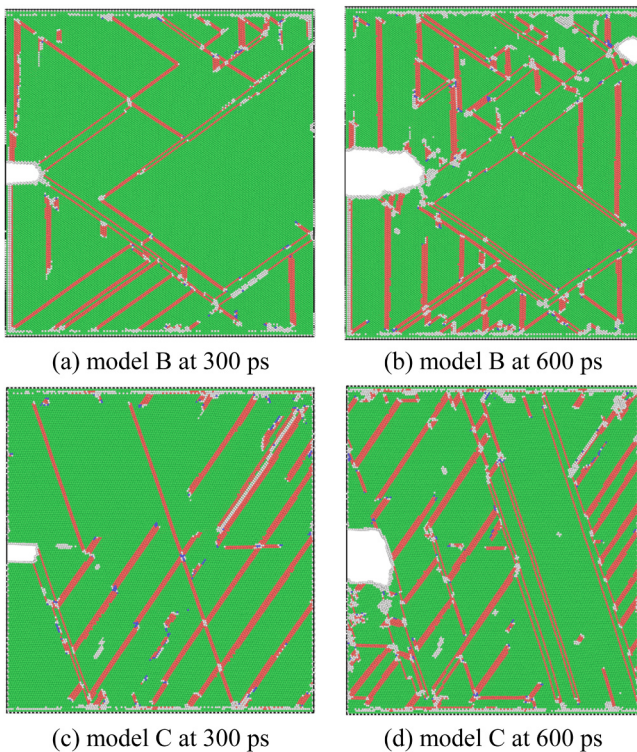


Fig. 7. The crack propagation for model B and model C, (a) CNA for model B at 300 ps, (b) CNA for model B at 600 ps, (c) CNA for model C at 300 ps, (d) CNA for model C at 600 ps.

stress alone to predict microstructural evolution could introduce errors.

Fig. 8(b) shows the plastic strain field of model B at 300 ps, where the plastic strain in model B (around 1.2) exceeded that of model A (around 0.7). Despite higher strain values, model B showed no clear void nucleation. This suggested that void nucleation is not only influenced by the magnitude of plastic strain but also by its local concentration. The calculated local strain concentration factors for models A and B, presented in **Fig. 8(c)** and (d), showed a maximum of 7.788 near the void region in model A and only 3.767 in model B. This disparity indicated that severe concentration of plastic strain is necessary for void nucleation. Regions with uniform plastic deformation, such as those resulting from dislocation slip at stacking faults, are less prone to void formation despite high absolute plastic strain values. In contrast, areas with highly concentrated plastic deformation, arising from intertwined dislocations, are more susceptible to void nucleation. The red circles in **Fig. 8** highlight areas of peak stress and plastic strain. During crack propagation, multiple peaks of stress and plastic strain were observed, with stress peaks being more dispersed and peaks of plastic strain concentrated at stacking faults and the crack tip. However, the peaks of plastic deformation concentration were only located at the crack tip, and these peaks delineated the areas where void nucleation occurred.

Fig. 9 shows the MD simulation result of model C at 300 ps, and **Fig. 7(c)(d)** show the corresponding CNA. In model C, partial dislocations nucleated at the crack tip and propagated along closely packed plane $(1\bar{1}\bar{1})$ with Burgers vectors $1/6[2\bar{1}1]$. As deformation intensified, a larger number of slip planes emerged and converged, resulting in significant blunting and numerous slip bands. However, similar to model B, model C showed minimal crack propagation and scarce void nucleation. **Fig. 9(a)** shows the stress field of model C at 300 ps, highlighting stress concentration at the crack tip. **Fig. 9(b)(c)** show the plastic strain field and local plastic strain concentration factor for model C. Compared with models A and B, model C exhibited lower plastic strain (0.397) and plastic strain concentration factor (3.333), suggesting a lower propensity for void nucleation. Red circles in **Fig. 9** show that the peak

concentration of plastic deformation is unique and located at the crack tip, which is indicative of potential areas for crack propagation.

The crack propagation behavior of single-crystal Ni is significantly influenced by crystallographic direction at the micro-nanoscale. Models with different crystal orientations exhibit varied plastic deformation patterns. For instance, some models, like model B, accumulate a large absolute value of plastic strain but lack a high local concentration, making them less prone to void formation and exhibiting subdued crack propagation. Conversely, models like model A, characterized by a high concentration of plastic strain, are more susceptible to void nucleation.

3.4. Crack propagation behavior for the in-plane shear process

The discussion above primarily addressed the influence of mode I loading conditions on the crack growth of single-crystal Ni. We further explored this by applying mode II loading to model A, comparing the crack propagation behavior between tensile and in-plane shear processes. External shear strain was applied to the negative x-direction surface (xy-plane) at a loading rate of $2 \times 10^8 \text{ s}^{-1}$ and an ambient temperature of 300 K. **Fig. 10** shows the CNA results of crystalline Ni from 180 to 600 ps ($0.036 \leq \gamma \leq 0.12$).

Fig. 10(a) shows that by 180 ps, under tensile strain, the model reached the yield point and began generating dislocations, with blunting dislocations appearing in the $1/6\langle 112 \rangle\{111\}$ slip systems. By 300 ps, as shown in **Fig. 10(b)**, interactions between two slip systems resulted in intersecting stacking faults of different orientations. At 600 ps, shown in **Fig. 10(c)**, these stacking faults increased, and there was a greater tendency for crack deflection following multiple dislocation emissions in the $1/6\langle 112 \rangle\{111\}$ slip systems, yet significant void generation was absent. The crack expansion and propagation in the shear process were less pronounced than in the tensile process under similar external strain loading.

Fig. 11 shows the stress distribution for von Mises stress and y-direction normal stress. Unlike the y-direction stress, which was not concentrated at the crack tip, von Mises stress concentrated around the tip and aligned closely with the defects (indicated by the green area in the figure). Under mode II loading conditions, von Mises stress predominantly influenced crack propagation. However, as indicated by red circles in **Fig. 11(d)(e)**, von Mises stress exhibited multiple concentration points, not solely at the crack propagation sites but also elsewhere within the configuration. Furthermore, **Fig. 11(f)** shows that the stress concentration region was located above the crack, not ahead of the crack tip (marked by red circles). Thus, relying solely on von Mises stress does not provide an accurate characterization of crack propagation behavior.

Here, we presented the results for plastic shear strain and its concentration factor under mode II loading conditions. **Fig. 12** shows that regions with substantial plastic shear strain and corresponding high concentration factors coincide with where the crack began to deform, making these parameters apt for studying mode II crack propagation. **Fig. 12(a)(b)(c)** show that while the shear strain around the crack tip was relatively large, it remained small compared to the values under mode I tensile loading. **Fig. 12(d)(e)(f)** show the distribution of the shear strain concentration factor at corresponding times, with a peak value of only 4.33. This suggested that the in-plane shearing process is less susceptible to localized accumulation of plastic deformation and less prone to void initiation. Consequently, crack propagation under mode II conditions is less pronounced than under mode I conditions. Furthermore, as demonstrated in **Fig. 12**, the peaks of plastic strain and its concentration occurring near the crack tip showed a clearer correspondence with defects compared to von Mises stress, indicating that these parameters are more effective for accurately predicting crack propagation behavior under mode II loading.

3.5. Analysis of crack growth behavior for different grain boundaries

Grain boundaries significantly influence crack propagation behavior,

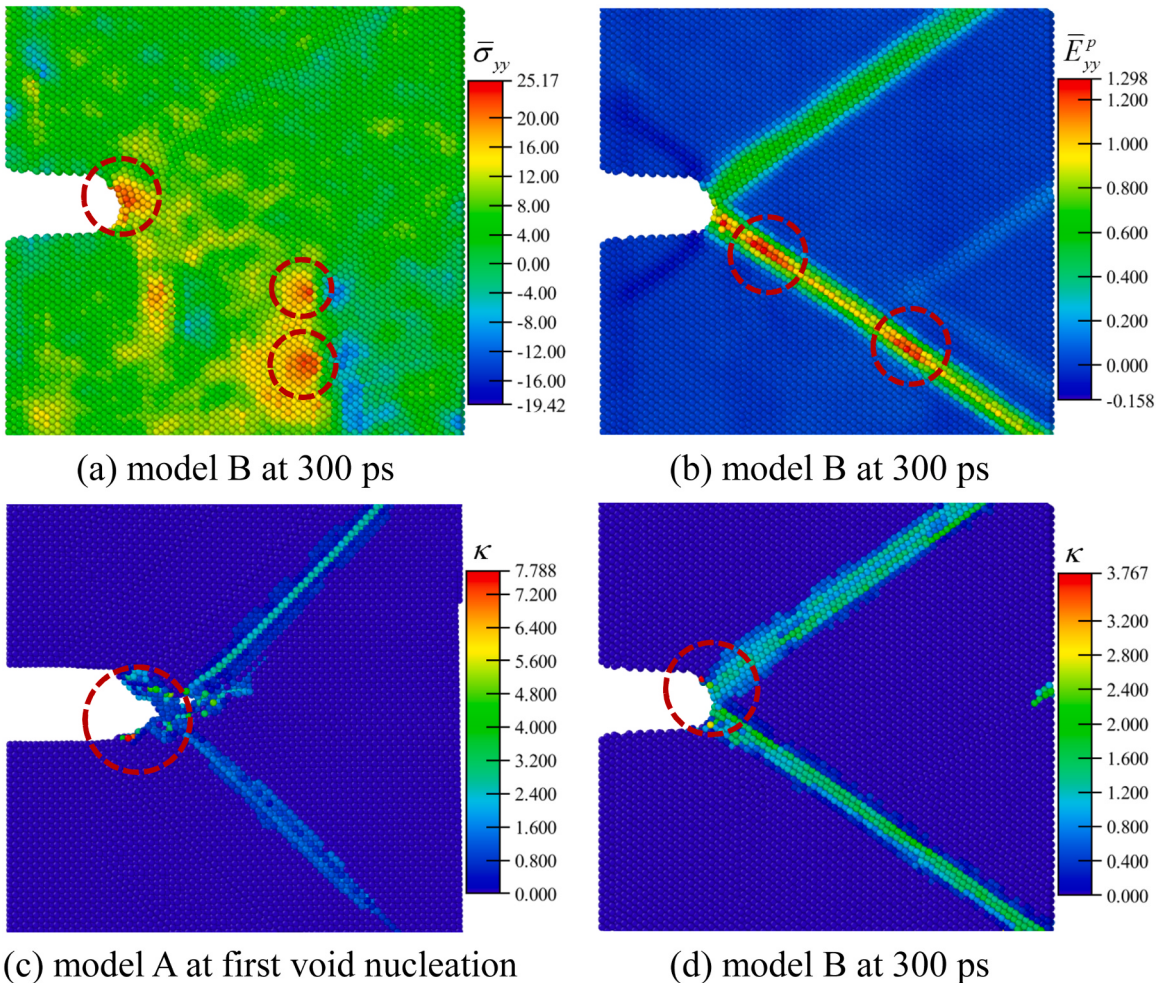


Fig. 8. The crack propagation for model B at 300 ps. (a) The stress field, (b) the plastic strain field, (d) the plastic strain concentration factor of model A (280 ps), (d) the plastic strain concentration factor of model B.

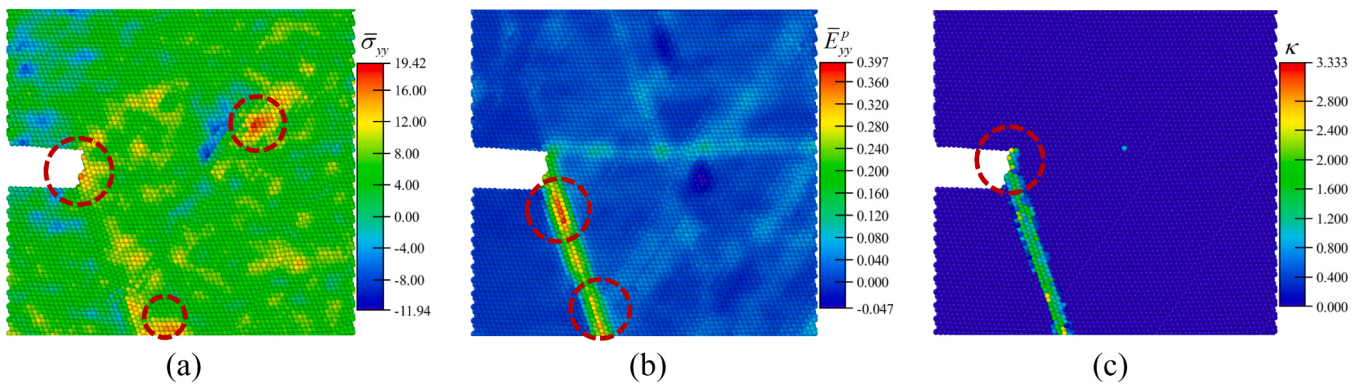


Fig. 9. The crack propagation for model C at 300 ps. (a) The stress field, (b) the plastic strain field, (c) the plastic strain concentration factor.

prompting the selection of three typical grain boundary models, D, E, and F, for study. These models are bi-crystals composed of two grains with differing orientations. Initially, the crystal orientation was [100] along the x-direction, [010] along the y-direction, and [001] along the z-direction. To create the variations, the right grain of each model was rotated by 10°: around the x-axis for model D, the y-axis for model E, and the z-axis for model F.

The tensile loading condition was used with a rate of $2 \times 10^8 \text{ s}^{-1}$ and an ambient temperature of 30 K. Fig. 13 shows the crack

propagation across the grain boundaries in bi-crystals, colored by CNA, where blue, green, and red represent BCC, FCC, and HCP structures respectively. The tensile loading was applied in the y-direction, perpendicular to the crack plane. In model D, the crack initially propagated rapidly, exhibiting more brittleness than ductility. By 340 ps, the crack had crossed the middle grain boundary, where plastic characteristics became more pronounced. The grain boundary formed by rotating the right grain around the x-axis significantly resisted crack propagation, with numerous defect structures at the crack tip and along the grain

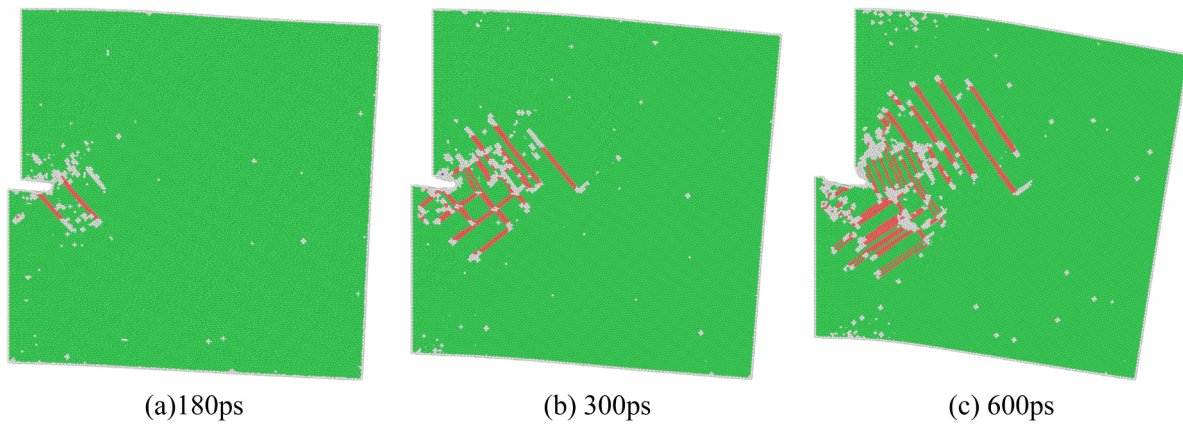


Fig. 10. The crack propagation for the mode II loading condition.

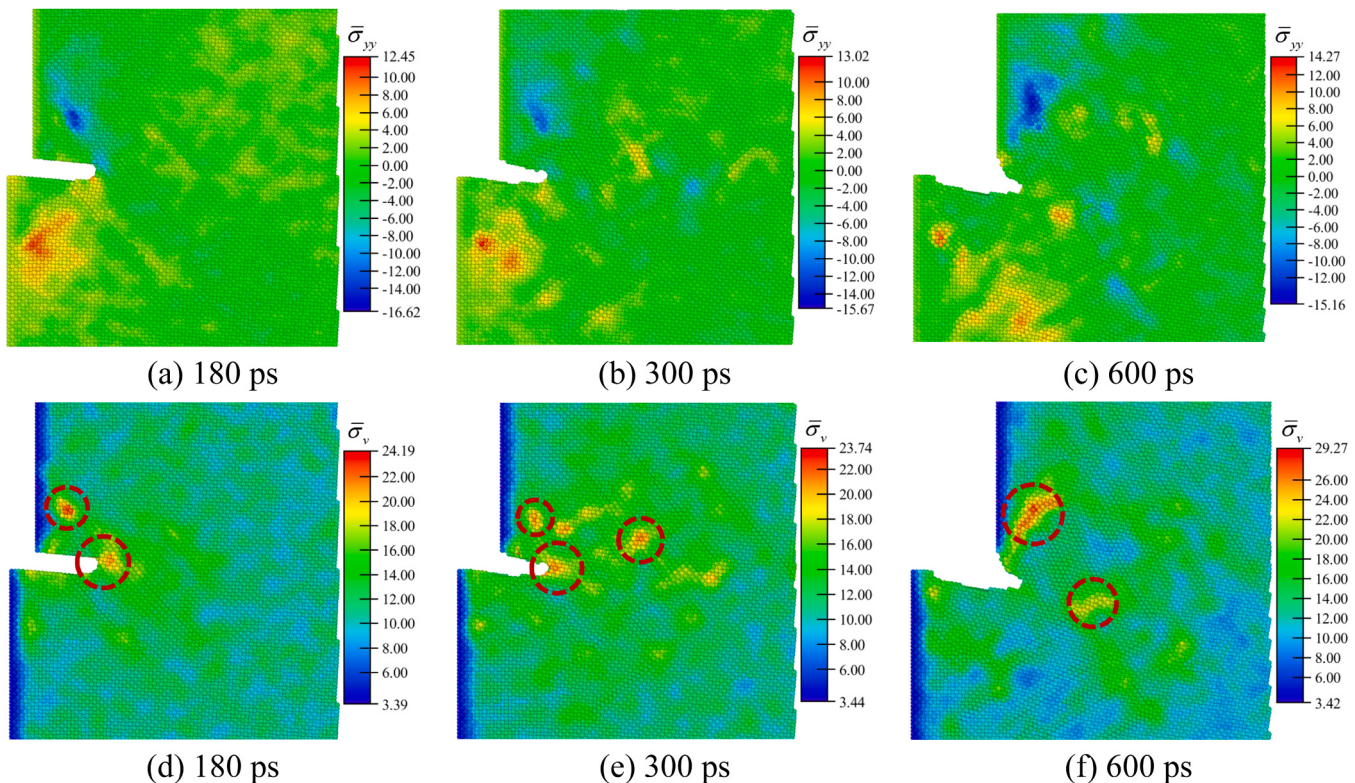


Fig. 11. The von Mises stress and y-direction normal stress around the crack tip. (a) The von Mises stress at 180 ps, (b) the von Mises stress at 300 ps, (c) the von Mises stress at 600 ps, (d) the y-direction tensile stress at 180 ps, (e) the tensile stress at 300 ps, (f) the tensile stress at 600 ps.

boundary, markedly slowing the crack's progress. Model E, like model D, initially showed brittle propagation, and then transitioned to obvious plastic characteristics. However, the plastic deformation at the crack tip in model E was more concentrated, allowing the crack to cross the grain boundary more easily by 340 ps. The grain boundary formed by rotation around the y-axis did not significantly inhibit crack growth. Fewer slip bands formed compared to model D. In model F, the middle grain boundary offered minimal resistance, and the crack crossed this boundary easily by 250 ps. The number of slip bands was minimal, and defect structures were present in a smaller range around the crack tip compared to models D and E. More plastic deformation accumulated around the tip, making crack growth in model F least affected by the middle grain boundary.

The study focused on crack propagation through grain boundaries, analyzing the distribution of stress, plastic strain, and plastic strain

concentration factor as cracks crossed the grain boundaries in three bicrystal models. Fig. 14 displays the results for models D, E, and F. We observed that rotation around the x-axis most effectively hindered crack propagation, followed by the y-axis, while z-axis rotation facilitated crack passage through the middle grain boundary. This difference was primarily due to varying boundary conditions among the models, which were periodic along the z-direction. Rotations around the x- and y-axes introduced periodic defects along the z-direction, unlike rotations around the z-axis. In model F (z-rotation), stress (20.99 GPa), plastic strain (0.88), and concentration factor (7.70) were the highest, indicating the most susceptibility to void nucleation. Conversely, models D (x-rotation) and E (y-rotation) exhibited lower values in these metrics, with rare void nucleation observed. Both models D and E showed similar stress and plastic strain levels (around 16 GPa and 0.6 respectively), but the concentration factor was higher in model E (6.84) compared to

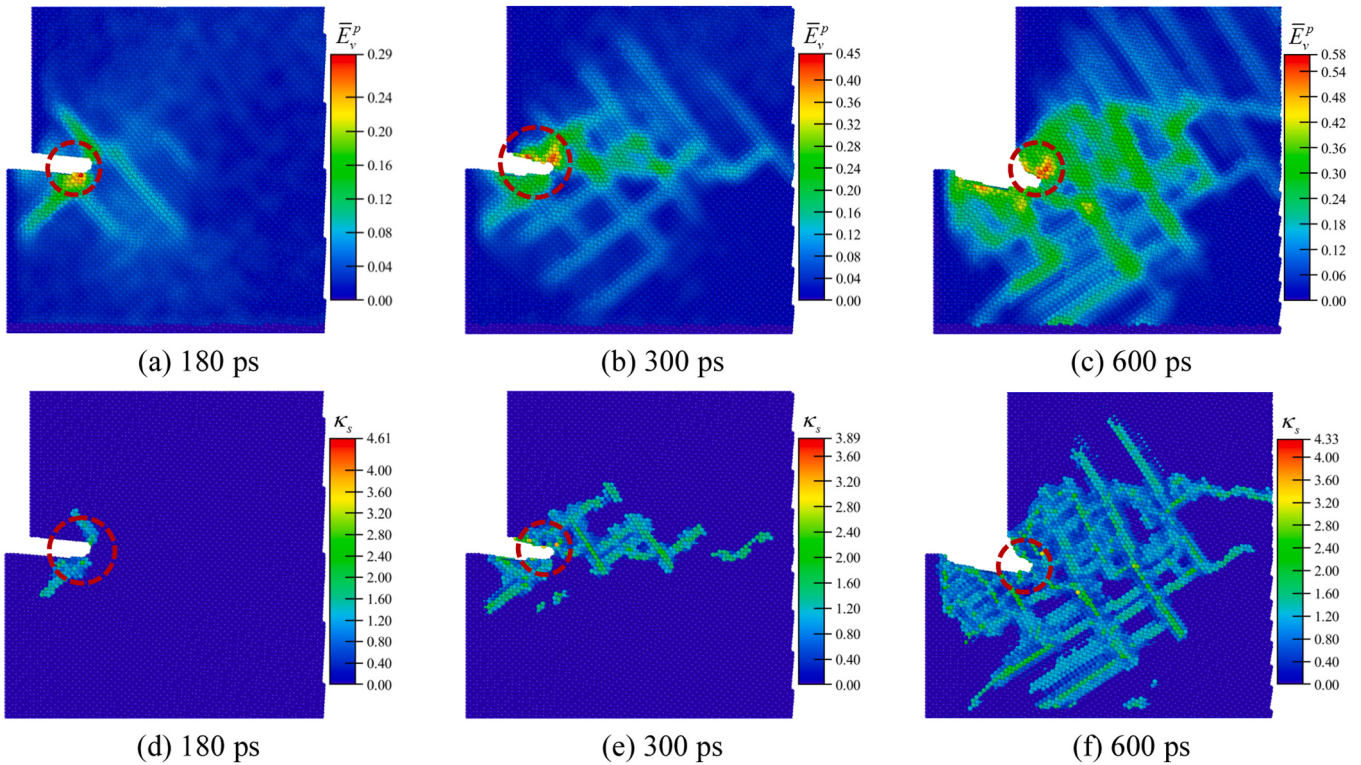


Fig. 12. The shear strain and the corresponding strain concentration factor around the crack tip. (a) The shear strain at 180 ps, (b) the strain at 300 ps, (c) the strain at 600 ps, (d) the shear strain concentration factor at 180 ps, (e) the concentration factor at 300 ps, (f) the concentration factor at 600 ps.

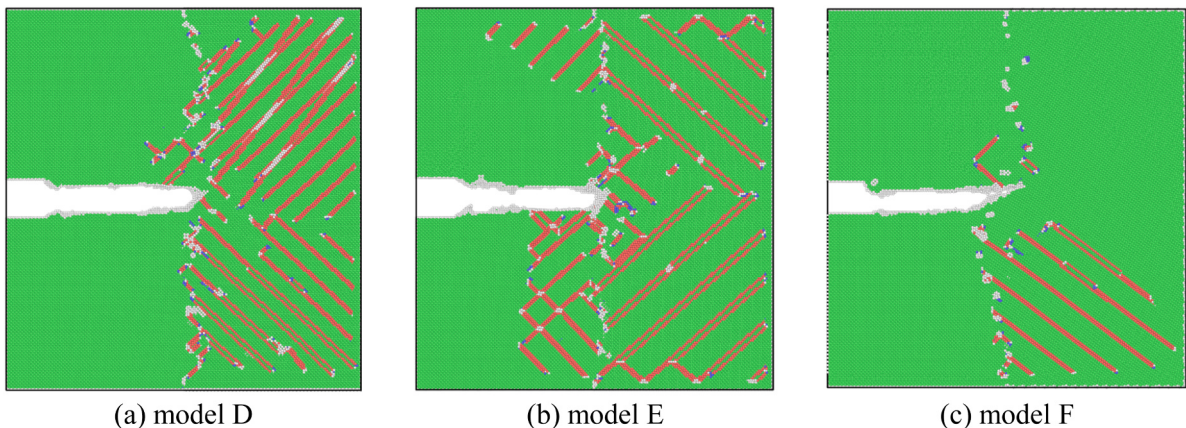


Fig. 13. The CNA results of bi-crystals. (a) Model D at 340 ps, (b) model E at 340 ps, (c) model F at 250 ps.

model D (5.31), linked to the orientation of periodic defects. Specifically, in model D, the defect distribution aligned with the crack propagation direction, resulting in the least plastic strain concentration at the crack tip and more slip bands around the tip, making the middle grain boundary in model D a significant barrier to crack propagation. Fig. 14 (a)(d)(g) highlight multiple stress peaks (red circles) in model D, E and F, and (d) reveals that peak stress of model E even did not occur at the crack tip, underscoring the inaccuracy of using stress alone to predict crack propagation. In contrast, plastic strains and concentration factors accurately located potential crack expansion areas.

3.6. Analysis of crack growth behavior for different grain sizes

We investigated the crack propagation behavior in polycrystalline Ni, specifically examining the impact of varying grain sizes. Grain sizes

of 8, 10, and 12 nm were selected as variables for models G, H, and I respectively, with experiments conducted at a temperature of 300 K and a loading rate of 2×10^8 s⁻¹. Fig. 15 shows the CNA results of these models at the first void generation. Fig. 15(a) shows model G at 303 ps, where noticeable blunting occurred near the crack tip. Numerous grain boundaries were in a slipping state, yet most grain structures remained intact. A void formed at the intersection of four grain boundaries and, as loading continued, connected with the existing crack and propagated along the grain boundaries. Fig. 15 (b) shows model H at 325 ps, where several stacking faults and other defects appeared near the crack tip. With fewer grain boundary structures, the phenomenon of grain boundary sliding diminished, leading to slip bands forming within the grains. In model H, a void initiated at the junction of three central grains and the crack continued to propagate along the grain boundaries. Fig. 15 (c) shows model I at 346 ps, numerous slip bands and unidentified defect

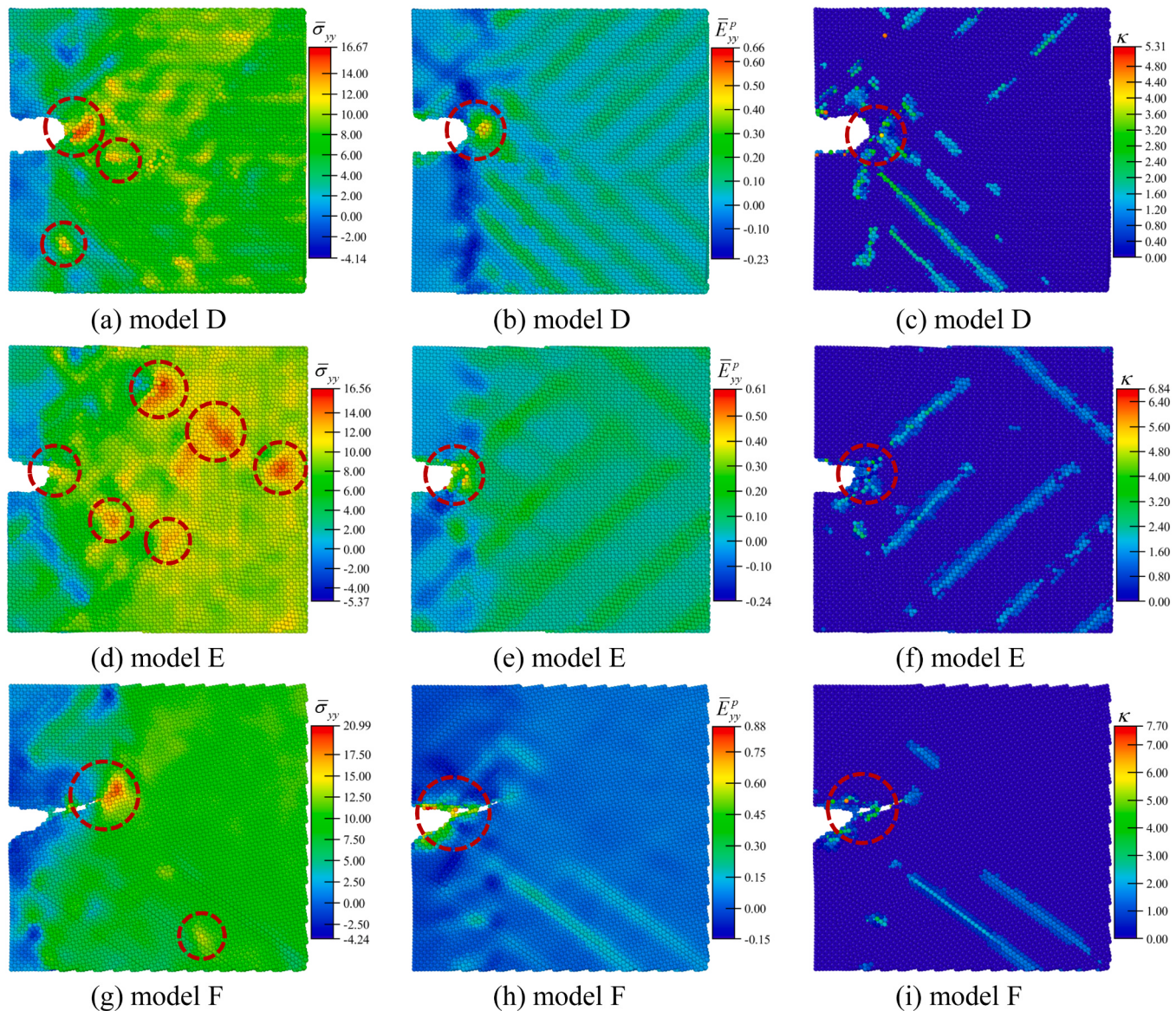


Fig. 14. The analysis of cracks propagating through grain boundaries. (a) The stress of model D, (b) the plastic strain of model D, (c) the plastic strain concentration factor of model D, (d) the stress of model E, (e) the plastic strain of model E, (f) the concentration factor of model E, (g) the stress of model F, (h) the plastic strain of model F, (i) the concentration factor of model F.

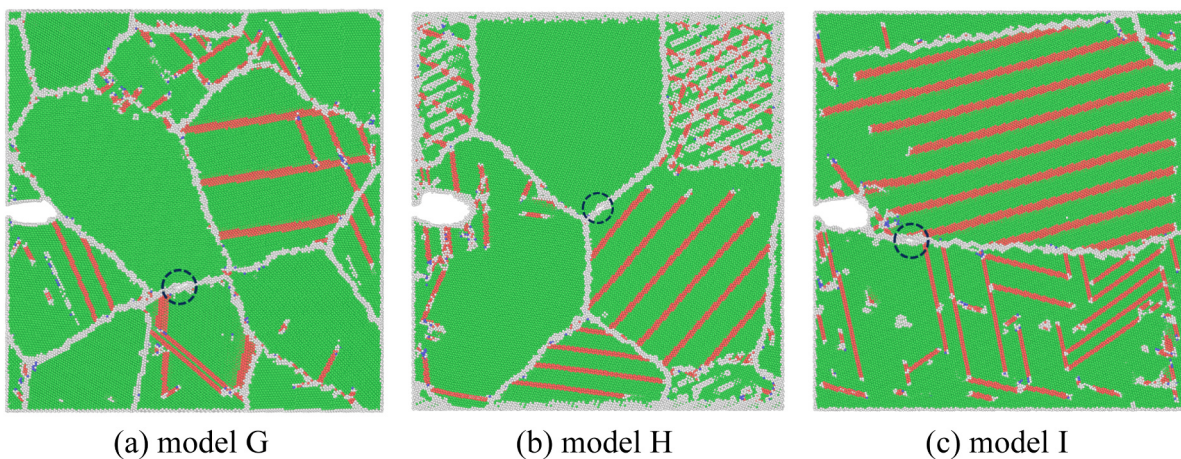


Fig. 15. The CNA results of polycrystals. (a) Model G at 306 ps, (b) model H at 327 ps, (c) model I at 350 ps, (Black circles are void locations).

structures around the tip. With the least grain boundary structures among the models, extensive slip bands formed on both sides of the grain boundaries in model I, indicating that dislocation gliding began to dominate the deformation process. Void generation occurred at the intersection of grain boundaries and slip bands, and expanded along the grain boundaries. The results indicated that in polycrystalline models, voids predominantly occurred at the junctions of multiple grains; the larger the grain size, the later the void nucleation.

In all three models, crack propagation was initiated by voids among grains. Fig. 16 shows the distribution of stress, plastic strain, and plastic strain concentration factor around the void generation sites. For the models with varying grain sizes, the limit values for stress, plastic strain, and plastic strain concentration factor were approximately 19 GPa, 0.5, and 4, respectively, suggesting that grain size had a minimal impact on these values due to the predominant mechanism of grain boundary slipping. Comparatively, the simulation results of model A (single crystal) showed that limit values for stress, plastic strain, and concentration factor for void nucleation at 300 K were 21 GPa, 0.7, and 7.7, respectively, with plastic deformation primarily driven by slip band

generation. The stress values for single crystals and polycrystals were similar, while the peak values for plastic strain and concentration factor in polycrystals were significantly lower. This indicated that grain boundaries in polycrystals are more susceptible to localized plastic deformation due to their fragility and propensity for slipping. Fig. 16(a)-(d)(g) shows that stress concentration occurred not only around the void and crack tip but also near some grain boundaries and stacking faults, demonstrating that using stress alone to predict crack propagation is insufficient (see red circles). Fig. 16(b)(c), (e)(f) and (h)(i) reveal that the peaks of plastic strain and concentration factor were located around the void generation site, offering a more accurate reflection of crack propagation dynamics.

3.7. Crack propagation dynamics

Crack propagation dynamics are crucial for understanding fracture behavior, with significant correlations observed between crack propagation and external conditions such as temperature, strain rate, and grain boundary characteristics. To further investigate these dynamics,

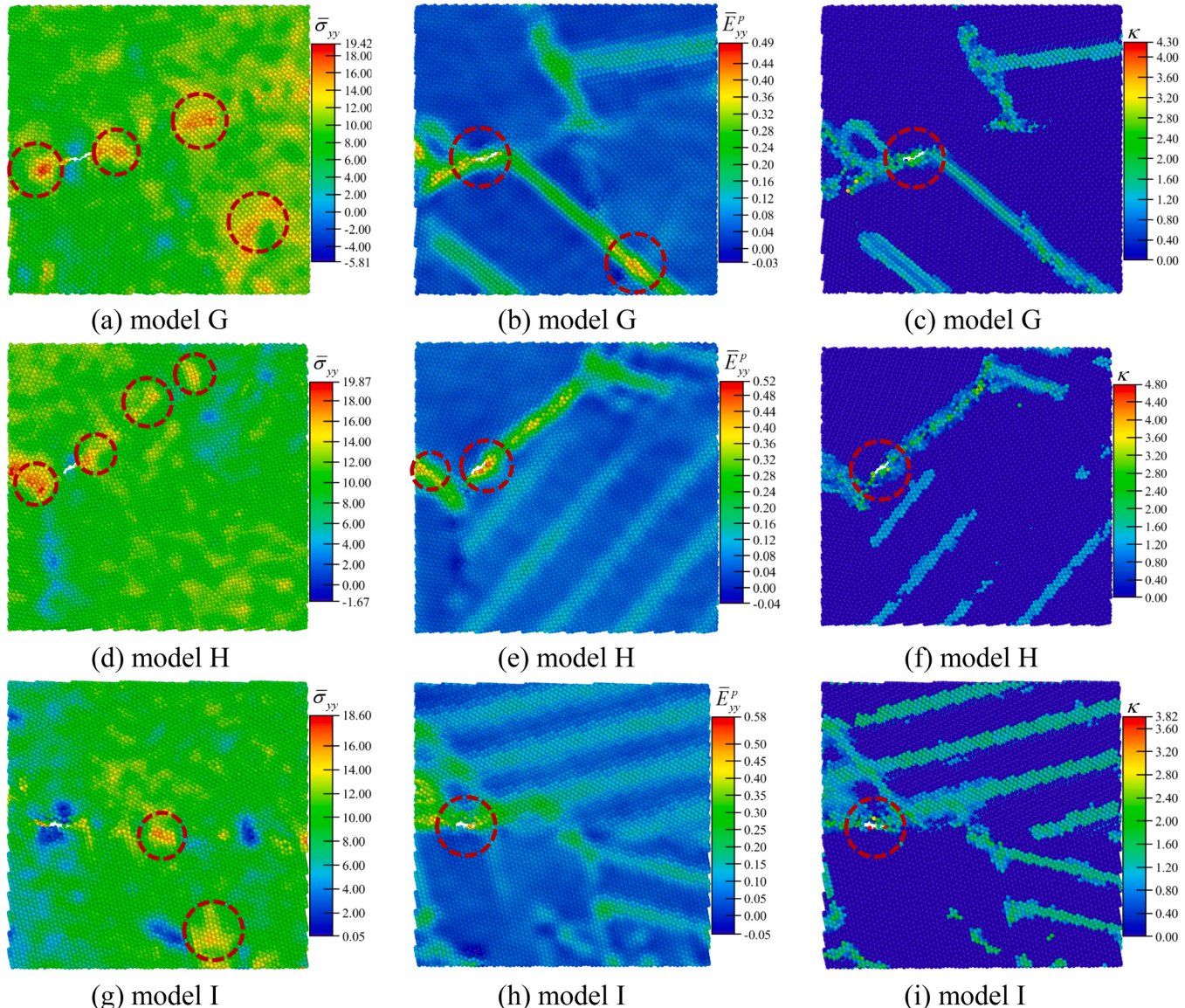


Fig. 16. Analysis of the first void nucleation. (a) The stress of model G, (b) the plastic strain of model G, (c) the plastic strain concentration factor of model G, (d) the stress of model H, (e) the plastic strain of model H, (f) the concentration factor of model H, (g) the stress of model I, (h) the plastic strain of model I, (i) the concentration factor of model I.

we analyzed the evolution of crack length under various temperatures, strain rates, and bi-crystal configurations.

Fig. 17(a) shows the relationship between crack length and loading strain across three different temperatures for model A. Prior to a loading strain of 0.36, crack growth rates showed minimal sensitivity to temperature changes. Beyond this threshold, temperature significantly influenced crack growth rates. At 0 K, crack propagation commenced around a strain of 0.4, exhibiting rapid progression and a brittle fracture response. At 30 K, thermal activation allowed crack initiation at a lower strain of 0.36, but the propagation rate slowed, transitioning towards ductile behavior, with a final crack length of 283.86 Å. At 300 K, crack growth started around a strain of 0.4 due to atomic motion randomness and was quickly arrested due to extensive dislocation formation ahead of the crack tip, resulting in a more ductile fracture response and a shorter final crack length of 254.99 Å. At 30 K and 300 K, the fastest propagation rates corresponded with significant plastic deformation and high local stress at the crack tip, facilitating easy void formation. However, when the crack reached a stable stage, despite high stress at the crack tip, the absence of significant plastic strain accumulation made void formation difficult, slowing crack propagation. This underscored the importance of considering not just stress distribution, but also plastic deformation and its concentration at the crack tip, in studying crack propagation dynamics.

Fig. 17(b) displays the crack length curves for model A across four strain rates. For all rates, the crack remained dormant until the loading strain exceeded 0.4, at which point it transitioned into rapid growth. The growth rate of the crack varied directly with the loading rates. At lower loading rates, the primary mechanism of plastic deformation was dislocation gliding, resulting in faster crack growth and a more distinct transition point, indicative of a brittle fracture response. At higher rates, the dominant deformation mechanism shifted to the formation of amorphous structures, leading to more plastic deformation at the crack tip and slower crack propagation. As crack growth approached stabilization, the final crack length was also clearly influenced by the loading rates. At a rate of 2×10^8 s⁻¹, the final crack length was 254.99 Å; at 4×10^8 s⁻¹, it was 230.70 Å; at 8×10^8 s⁻¹, it was 193.47 Å; and at 2×10^9 s⁻¹, it was 146.30 Å. The trend showed that higher loading rates resulted in shorter crack lengths, primarily because increased rates heighten the plasticity threshold at the crack tip, thereby reducing the likelihood of void formation.

Fig. 17(c) shows crack propagation rate curves for three bi-crystal models. In model F (z-rotation), the two grains exhibited consistent periodicity in the z-direction. The crack tip was more prone to accumulate plastic deformation, resulting in the fastest propagation and the longest final crack length. In model E (y-rotation), the periodic defects on the z-direction boundary were perpendicular to the crack direction, facilitating void generation across the grain boundary and resulting in a

slightly smaller crack growth rate and final length. In model D (x-rotation), the periodic defects on the z-boundary aligned with the crack direction, minimizing plastic deformation concentration at the tip and enhancing the middle grain boundary's impediment to crack propagation. Consequently, model D exhibited the slowest crack growth rate and the shortest final crack length.

4. Conclusion

We enhanced the existing atomic strain calculation method by introducing a new technique for selecting neighboring atoms, enabling precise computation of atomic strain near defects like voids and surfaces. Additionally, we proposed a new parameter to consistently measure the local concentration of plastic deformation across different crystallographic directions. Subsequent MD simulations investigated the effects of temperature, strain rate, crystallographic direction, loading mode, grain boundary, and grain size on crack propagation in Ni plates, with a focus on the evolution of stress, plastic strain and microstructures near propagating cracks. Key conclusions include:

- (1) **Plastic Deformation:** Void nucleation requires not only stress concentration but also significant local plastic deformation. Long-range effects of dislocation gliding and twinning are insufficient without substantial local accumulation.
- (2) **Temperature Dependence:** At 0 K, cracks propagated rapidly in a brittle manner with minimal plastic deformation at the tip. At higher temperatures (30 and 300 K), crack propagation involved void nucleation, growth, and coalescence, with the plasticity limit increasing and the stress limit slightly decreasing.
- (3) **Strain Rate Influence:** Similar to temperature effects, higher strain rates increased the plasticity limit but decreased the stress limit, indicating strain softening.
- (4) **Crystallographic Direction:** The ⟨100⟩ crystal orientation supported significant crack propagation due to localized plastic deformation at the crack tip surpassing a critical threshold, whereas ⟨110⟩ and ⟨111⟩ orientations showed limited plastic accumulation, resulting in minimal crack propagation.
- (5) **Loading Mode Differences:** The xz in-plane shear process differed markedly from y-direction tensile loading. In tensile loading, stress concentrated more at the crack tip, increasing the likelihood of void formation, while in-plane shear showed less pronounced crack propagation despite visible slip bands.
- (6) **Bi-Crystal Grain Boundaries:** The middle grain boundary's impact on crack propagation varied with the z-direction defects conditions of the grains. The x-rotation grain boundary hindered crack propagation due to low plastic deformation concentration, the y-rotation facilitated void formation, and the z-rotation

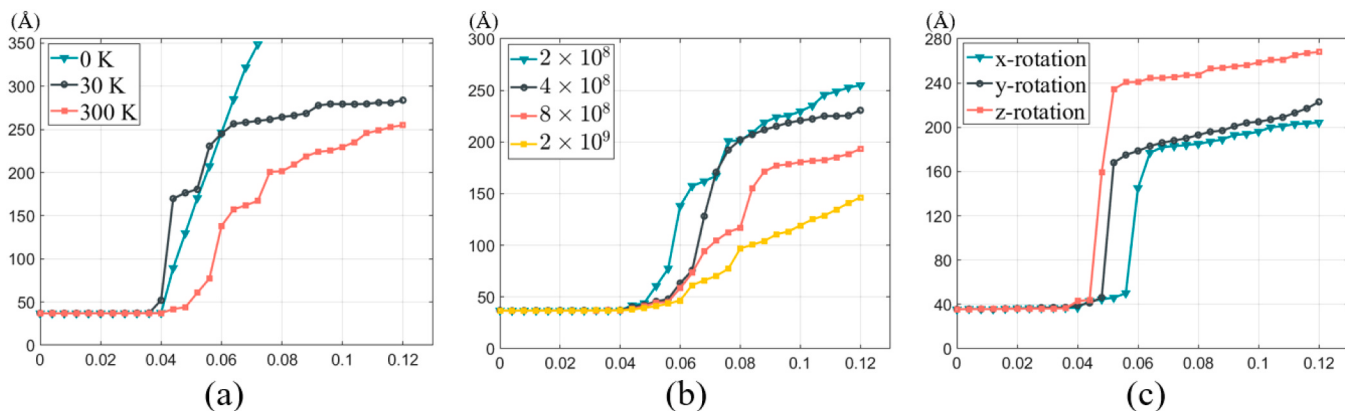


Fig. 17. The relationship between crack length and strain (x-axis: strain, y-axis: crack length (Å)). (a) Crack lengths for different temperatures, (b) crack lengths for different strain rates, (c) crack lengths for different bi-crystals.

- allowed cracks to cross easily due to the two grains matching the same periodic conditions in the z-direction.
- (7) **Grain Size in Polycrystals:** Smaller grain sizes (8–12 nm) led to faster crack propagation due to significant plastic accumulation and high plastic strain concentration at grain boundaries. Compared to single crystals, polycrystals showed significantly lower peak values of plastic strain and strain concentration at grain boundaries, indicating less stability within the grain boundary structures.

CRediT authorship contribution statement

Yifan Yu: Writing – review & editing, Writing – original draft, Visualization, Validation, Methodology, Investigation, Formal analysis, Conceptualization. **Yipeng Rao:** Writing – review & editing, Validation.

Declaration of Competing Interest

The authors declare the following financial interests/personal relationships which may be considered as potential competing interests: Yifan Yu reports financial support was provided by National Natural Science Foundation of China. If there are other authors, they declare that they have no known competing financial interests or personal relationships that could have appeared to influence the work reported in this paper.

Data availability

Data will be made available on request.

Acknowledgments

This work is supported by the Computational Dynamics Lab of the School of Aerospace Engineering at Tsinghua University, the High Performance Computing Center at Tsinghua University, and the State Key Laboratory of Scientific and Engineering Computing at the Chinese Academy of Sciences.

References

- [1] K. Nishimura, N. Miyazaki, Molecular dynamics simulation of crack growth under cyclic loading, *Comput. Mater. Sci.* 31 (3) (2004) 269–278.
- [2] M.J. Buehler, H. Gao, Y. Huang, Atomistic and continuum studies of stress and strain fields near a rapidly propagating crack in a harmonic lattice, *Theor. Appl. Fract. Mech.* 41 (1) (2004) 21–42.
- [3] R. Matsumoto, et al., Molecular-dynamics study on crack growth behavior relevant to crystal nucleation in amorphous metal, *Comp. Model. Eng. Sci.* 9 (1) (2005).
- [4] M. Karimi, T. Roarty, T. Kaplan, Molecular dynamics simulations of crack propagation in Ni with defects, *Model. Simul. Mater. Sci. Eng.* 14 (8) (2006) 1409.
- [5] Y.-F. Guo, D.-L. Zhao, Atomistic simulation of structure evolution at a crack tip in bcc-iron, *Mater. Sci. Eng.: A* 448 (1) (2007) 281–286.
- [6] Y.-F. Guo, et al., Mechanisms of martensitic phase transformations in body-centered cubic structural metals and alloys: molecular dynamics simulations, *Acta Mater.* 55 (19) (2007) 6634–6641.
- [7] Y.-F. Guo, Y.-S. Wang, D.-L. Zhao, Atomistic simulation of stress-induced phase transformation and recrystallization at the crack tip in bcc iron, *Acta Mater.* 55 (1) (2007) 401–407.
- [8] S. Xu, X. Deng, Nanoscale void nucleation and growth and crack tip stress evolution ahead of a growing crack in a single crystal, *Nanotechnology* 19 (11) (2008) 115705.
- [9] H. Krull, H. Yuan, Suggestions to the cohesive traction–separation law from atomistic simulations, *Eng. Fract. Mech.* 78 (3) (2011) 525–533.
- [10] W.-P. Wu, Z.-Z. Yao, Molecular dynamics simulation of stress distribution and microstructure evolution ahead of a growing crack in single crystal nickel, *Theor. Appl. Fract. Mech.* 62 (2012) 67–75.
- [11] J. Zhang, S. Ghosh, Molecular dynamics based study and characterization of deformation mechanisms near a crack in a crystalline material, *J. Mech. Phys. Solids* 61 (8) (2013) 1670–1690.
- [12] L. Ma, et al., Molecular dynamics simulation of fatigue crack propagation in bcc iron under cyclic loading, *Int. J. Fatigue* 68 (2014) 253–259.
- [13] P.-H. Sung, T.-C. Chen, Studies of crack growth and propagation of single-crystal nickel by molecular dynamics, *Comput. Mater. Sci.* 102 (2015) 151–158.
- [14] R.-Z. Qiu, C.-C. Li, T.-H. Fang, Mechanical properties and crack growth behavior of polycrystalline copper using molecular dynamics simulation, *Phys. Scr.* 92 (8) (2017) 085702.
- [15] H. Ji, et al., Molecular dynamics simulation of the interaction between cracks in single-crystal aluminum, *Mater. Today Commun.* 30 (2022) 103020.
- [16] L. Ya-zhou, et al., Molecular dynamics simulation of phase transition and crack propagation in metastable high entropy alloy, *Mater. Today Commun.* 33 (2022) 104642.
- [17] A.J. Cao, Y.G. Wei, Molecular dynamics simulation of plastic deformation of nanotwinned copper, *J. Appl. Phys.* 102 (8) (2007) 083511.
- [18] L.A. Zepeda-Ruiz, et al., Probing the limits of metal plasticity with molecular dynamics simulations, *Nature* 550 (7677) (2017) 492–495.
- [19] M. Nikolić, et al., Crack propagation in dynamics by embedded strong discontinuity approach: Enhanced solid versus discrete lattice model, *Comput. Methods Appl. Mech. Eng.* 340 (2018) 480–499.
- [20] Y. Zhou, Z. Yang, Z. Lu, Dynamic crack propagation in copper bicrystals grain boundary by atomistic simulation, *Mater. Sci. Eng.: A* 599 (2014) 116–124.
- [21] Y. Zhang, et al., A molecular dynamics study of intercrystalline crack propagation in nano-nickel bicrystal films with (010) twist boundary, *Eng. Fract. Mech.* 168 (2016) 147–159.
- [22] L. Chang, T. Kitamura, C.-Y. Zhou, Atomic simulation of the orientation effects on crack tip behavior in titanium single crystal, *Theor. Appl. Fract. Mech.* 110 (2020) 102791.
- [23] Z. Xing, H. Fan, G. Kang, Molecular dynamics simulations on the intergranular crack propagation of magnesium bicrystals, *Comput. Mater. Sci.* 210 (2022) 111058.
- [24] Y. Yu, J. Cui, Elastic–plastic deformation decomposition algorithm for metal clusters at the atomic scale, *Comput. Mech.* 67 (2) (2021) 567–581.
- [25] A. Stukowski, Visualization and analysis of atomistic simulation data with OVITO—the Open Visualization Tool, *Model. Simul. Mater. Sci. Eng.* 18 (1) (2010) 015012.
- [26] Y. Yu, J. Cui, Quantification of the atomic surfaces and volumes of a metal cluster based on the molecular surface model, *Phys. Scr.* 98 (4) (2023) 045704.
- [27] C.B. Cui, H.G. Beom, Molecular dynamics simulations of edge cracks in copper and aluminum single crystals, *Mater. Sci. Eng.: A* 609 (2014) 102–109.
- [28] F. Shimizu, S. Ogata, J. Li, Theory of shear banding in metallic glasses and molecular dynamics calculations, *Mater. Trans.* 48 (11) (2007) 2923–2927.
- [29] M.L. Falk, J.S. Langer, Dynamics of viscoplastic deformation in amorphous solids, *Phys. Rev. E* 57 (6) (1998) 7192–7205.